ARTICLES
https://doi.org/10.1038/s41560-022-00985-z

nature energy

Understanding what limits the voltage of polycrystalline CdSeTe solar cells

Arthur Onno[1]✉, Carey Reich[2], Siming Li[3], Adam Danielson[2], William Weigand[1], Alexandra Bothwell[3], Sachit Grover[4], Jeff Bailey[4], Gang Xiong[4], Darius Kuciauskas[3], Walajabad Sampath[2] and Zachary C. Holman[1]✉

The origin of voltage deficits in polycrystalline cadmium selenide telluride (CdSeTe) solar cells is unclear. Here, we present a comprehensive voltage loss analysis performed on state-of-the-art CdSeTe devices—fabricated at Colorado State University and First Solar—using photoluminescence techniques, including external radiative efficiency (ERE) measurements. More specifically, we report the thermodynamic voltage limit $V_{oc,ideal}$, internal voltage iV_{oc} and external voltage V_{oc} of partially and fully finished cells fabricated with different dopant species, dopant concentrations and back contacts. Arsenic-doped aluminium-oxide-passivated cells made at Colorado State University present remarkably high ERE (>1%)—translating into iV_{oc} above 970 mV—but suffer from poor back-contact selectivity. On the other hand, arsenic-doped devices from First Solar present almost perfect carrier selectivity ($V_{oc} = iV_{oc}$), leading to V_{oc} above 840 mV, and are limited by recombination in various parts of the device. Thus, development of contact structures that are both passivating and selective in combination with highly luminescent absorbers is key to reducing voltage losses.

Recent material improvements in polycrystalline cadmium telluride (CdTe) photovoltaic solar cells have increased both the effective minority-carrier lifetime, τ, and the acceptor (activated p-type dopant) concentration, N_A. In particular, alloying CdTe with selenium (CdSeTe) has led to an increase in τ from a few nanoseconds to tens of nanoseconds[1,2]. Further, metal-oxide-passivation layers, such as aluminium oxide (Al_2O_3) and magnesium zinc oxide (MZO), can reduce recombination at the front and back interfaces, resulting in surface recombination velocities below 100 cm s^{-1} and lifetimes well above 100 ns (refs. [3–6]). Finally, arsenic doping has led to $N_A > 10^{16}$ cm^{-3}, along with higher performance stability and lower degradation rates, thanks to reduced carrier compensation when compared with conventional copper-doped devices[7–10].

Despite these materials innovations, the voltage and, consequently, the efficiency of polycrystalline CdSeTe devices remain low: the open-circuit voltage, V_{oc}, of record-efficiency devices is still below 900 mV and, thus, the band gap–voltage offset $E_g/q - V_{oc}$, where E_g is the absorber's bandgap and q is the elementary charge, exceeds 500 mV. In comparison, record band gap–voltage offsets are below 350 mV for competing thin-film technologies, such as perovskite and gallium arsenide (GaAs), and below 400 mV for the best industrial crystalline silicon solar cells[11–13]. Thus, despite being the second-most manufactured solar cell technology, CdSeTe still has the largest scope for improvement. Device modelling indicates that these high bulk lifetimes, high acceptor concentrations and low surface recombination velocities should, together, enable open-circuit voltages in excess of 1 V and efficiencies above 24% (refs. [14–16]). This mismatch between model predictions and experimental results raises the question of what limits the voltage of polycrystalline CdSeTe solar cells.

In particular, it remains unclear what the theoretical voltage limit $V_{oc,ideal}$ of CdSeTe absorbers is, and how Se alloying and As doping affect this limit; what the internal voltage, iV_{oc} (or quasi-Fermi-level splitting: QFLS = $q \times iV_{oc}$), of long-lifetime, high acceptor concentration CdSeTe devices with passivated surfaces is; and, finally, to what extent selectivity losses reduce the open-circuit voltage from iV_{oc} to V_{oc}. In the crystalline silicon community, these questions are routinely answered to guide the development of high-efficiency devices using techniques such as quasi-steady-state photoconductance[17,18]. Similar techniques, often based on quantitative photoluminescence measurements, are now emerging for non-silicon thin-film devices, particularly perovskite solar cells[19–22].

Here, we answer these questions for CdSeTe samples fabricated using a range of process conditions, doping strategies (As or Cu) and contact structures. We calculate $V_{oc,ideal}$ and compare it with iV_{oc}, obtained from external radiative efficiency (ERE) measurements, and V_{oc}. We show how sub-band-gap features can substantially reduce $V_{oc,ideal}$ by increasing the absorbed blackbody photon current with correspondingly negligible increases in the photogenerated current under illumination. This effect is particularly detrimental in As-doped samples and in the presence of a highly reflective back contact. We then parse the voltage losses of finished devices into contributions due to sub-band-gap features, to non-radiative recombination and to imperfect selectivity. We show how Colorado State University's Cu-doped devices with a conventional Te back contact exhibit a decent selectivity—with V_{oc} approaching iV_{oc}—but are limited by non-radiative recombination. Conversely, As-doped devices with a passivating back contact can exhibit a very high iV_{oc} (>970 mV) but suffer from poor selectivity, leading to low V_{oc} (<500 mV). Finally, we show how, in As-doped samples fabricated at First Solar, the As doping drives the selectivity, with the selectivity metric, $S_{oc} = V_{oc}/iV_{oc}$, reaching a value of 1 when the doping is high enough. Our work uncovers which metrics researchers should use and which areas of research should be prioritized to reduce voltage losses.

[1]School of Electrical, Computer and Energy Engineering, Arizona State University, Tempe, AZ, USA. [2]Department of Mechanical Engineering, Colorado State University, Fort Collins, CO, USA. [3]National Renewable Energy Laboratory, Golden, CO, USA. [4]California Technology Center, First Solar Inc., Santa Clara, CA, USA. ✉e-mail: arthur.onno@asu.edu; zachary.holman@asu.edu

Breakdown of voltage losses and device structures. The open-circuit voltage of a photovoltaic device is given by its maximum theoretical value reduced by (non-radiative) recombination and contact selectivity losses. According to detailed balance analysis, the theoretical voltage limit $V_{oc,ideal}$ is

$$V_{oc,ideal} = \frac{k_B T}{q} \ln\left(\frac{\int a(\lambda)\,\phi_{exc}(\lambda)\,d\lambda}{\int a(\lambda)\,\phi_{BB}(\lambda, T)\,d\lambda} + 1\right) \quad (1)$$

where k_B is the Boltzmann constant, T is the sample temperature, q is the elementary charge, λ is the wavelength, $a(\lambda)$ is the sample's absorptance, $\phi_{exc}(\lambda)$ is the excitation photon current and $\phi_{BB}(\lambda, T)$ is the blackbody photon current[23,24]. As detailed in Supplementary Discussion 1, under standard test conditions (ϕ_{exc} = AM1.5G illumination, T = 298.15 K), $V_{oc,ideal}$ depends only on the absorptance of the sample—specifically on the position and sharpness of the band edge, as tail states and sub-band-gap features can reduce the effective band gap of the sample[25–27]. In real devices, non-radiative recombination—quantified by the ERE—reduces the QFLS from the theoretical limit $q \times V_{oc,ideal}$. (For the sake of consistency across the photovoltaics community, in the remainder of this paper we refer to the QFLS as the *internal* or *implied* voltage iV_{oc}: QFLS = $q \times iV_{oc}$). The internal voltage iV_{oc} is then given by (Supplementary Discussion 2):[28,29]

$$iV_{oc} = V_{oc,ideal} - \frac{k_B T}{q} |\ln(ERE)|. \quad (2)$$

The recent lifetime and acceptor concentration improvements in CdSeTe contribute to reducing non-radiative recombination—thus enhancing ERE and consequently iV_{oc}—even though iV_{oc} has not historically been tracked and reported by the CdSeTe community. Finally, selectivity losses, due to the non-zero resistances experienced by electrons and holes as they travel through the absorber and out of the contact layers, are responsible for the difference between the internal voltage iV_{oc} and the external voltage V_{oc}:

$$V_{oc} = S_{oc} \times iV_{oc}, \quad (3)$$

with $S_{oc} = V_{oc}/iV_{oc}$ being the selectivity metric of the device (Supplementary Discussion 3)[28,30,31].

To investigate the roles played by material properties—especially absorber doping—and contact passivation in voltage losses, we fabricated multiple batches of devices over two years, varying the dopant species and doping technique (Cu diffusion post-deposition or in situ As doping), the structure of the absorber (thickness of the CdSeTe and CdTe layers, percentage of Se in the CdSeTe source material), the process parameters (for example, deposition temperature, $CdCl_2$ treatment duration) and the type of back contact, as summarized in Fig. 1a. Unless specified, the absorber was formed by deposition of a CdSeTe/CdTe bilayer, with the subsequent chlorination treatment causing partial diffusion of Se towards the back of the sample, thus yielding a graded band gap absorber[32]. Samples with varying levels of As doping were also provided by First Solar for comparison.

MZO electron-contact layers can provide good interfacial passivation, with an interface recombination velocity below 200 cm s^{-1}, and are thus unlikely to cause a sizeable drop in iV_{oc}[3,6]. The conventional Te-based back hole-contact structure used at Colorado State University, on the other hand, is probably responsible for substantial recombination, as Te is a narrow band gap semiconductor (E_g < 0.4 eV) in direct contact with the CdSeTe absorber. Hereafter we refer to this contact structure as the 'baseline' contact. As an alternative, we used passivating back-contact structures consisting of a thin (≈2 nm) layer of aluminium oxide (Al_2O_3)—to passivate the back interface—followed by a p-type boron-doped hydrogenated amorphous silicon (a-Si:H(p)) layer[33]. Similar hole contacts combining a passivation layer together with an a-Si:H(p) hole-selective layer have been used to reach V_{oc} > 1 V in monocrystalline CdTe devices[34]. This substitute Al_2O_3/a-Si:H(p) contact structure, which we refer to as a 'passivating' contact, is capped off with an indium tin oxide/silver (ITO/Ag) electrode, as is used in silicon heterojunction solar cells[35].

Effect of dopants and cell optics on sub-band gap features. As shown in Fig. 1b, these device structures exhibit different sub-band gap absorption and emission behaviours and, thus, different $V_{oc,ideal}$. The trends shown in these four characteristic devices have been repeatedly observed across many samples, both from direct photoluminescence (PL) measurement and from reconstruction of the emission spectrum from external quantum efficiency (EQE) measurements (see Supplementary Discussion 1 and Supplementary Methods 1 for details on reconstruction of the emission spectrum). All the samples exhibit some form of sub-band-gap features, including the Cu-doped sample with a baseline Te back contact, even though in that case the effect on $V_{oc,ideal}$ is minimal. Such sub-band-gap behaviours are not usually observed in unalloyed monocrystalline CdTe devices[36,37]. However, sub-band-gap emission has been associated with Se-related states within the band gap in Se-alloyed polycrystalline CdSeTe samples[2].

Notably, both the passivating back contact and As doping lead to an increase in sub-band-gap features. The increase in sub-band-gap absorption with As doping has been previously documented and associated with electrostatic potential fluctuations, band gap fluctuations and carrier concentration fluctuations due to compensating donors and acceptors[8,38,39]. To confirm that As doping is responsible for the observed increase in sub-band-gap features, we analysed CdSeTe samples with increasing As concentration provided by First Solar, shown in Fig. 1c. Although the shape of the sub-band-gap features is different from that of samples fabricated at Colorado State University, their amplitude increases strongly with As concentration, leading to a substantial decrease in $V_{oc,ideal}$, as shown in Supplementary Table 3 and Supplementary Data 1. However, the ERE, shown in the inset in Fig. 1c, and the iV_{oc} do not follow such a monotonic trend; at lower concentrations, more As is slightly beneficial, but this trend reverses at higher concentrations, probably as a result of increased carrier compensation (lower dopant activation) with increasing As doping[9]. The influence of As doping is further confirmed by samples fabricated at Colorado State University; the As-doped samples shown in Fig. 1b, deposited from a lower As-concentration source material, exhibit less severe sub-band-gap features than the devices shown in Fig. 1d, which were deposited from a higher As-content source material.

Although the increase in sub-band-gap features when switching from Cu to As doping can be traced to the change in the material properties of the absorber, this is not the case for the type of back contact used. Given that these back contacts are deposited with a low thermal budget after the $CdCl_2$ chlorination and Cu-doping steps (if the latter is included), it is unlikely that the material properties of the absorber are affected by the back contact. Conversely, as we have recently shown, the optics of the cell are strongly altered when using our passivating back-contact architecture, as the Ag electrode acts as a back reflector—whereas the baseline Te back contact is highly absorptive—leading to at least a doubling of the path length for long-wavelength photons[40]. As shown in Fig. 1d and in Supplementary Table 4, the increase in back reflectance with each additional layer of the passivating contact stack leads to an augmentation of sub-band-gap features—as the average path length of long-wavelength photons is increased—along with an increase in ERE—as the escape probability of emitted photons through the front of the device is enhanced when the absorptance of the back contact decreases. Here, the increase in sub-band-gap features—and the associated decrease in $V_{oc,ideal}$ (but increase in iV_{oc})—are due

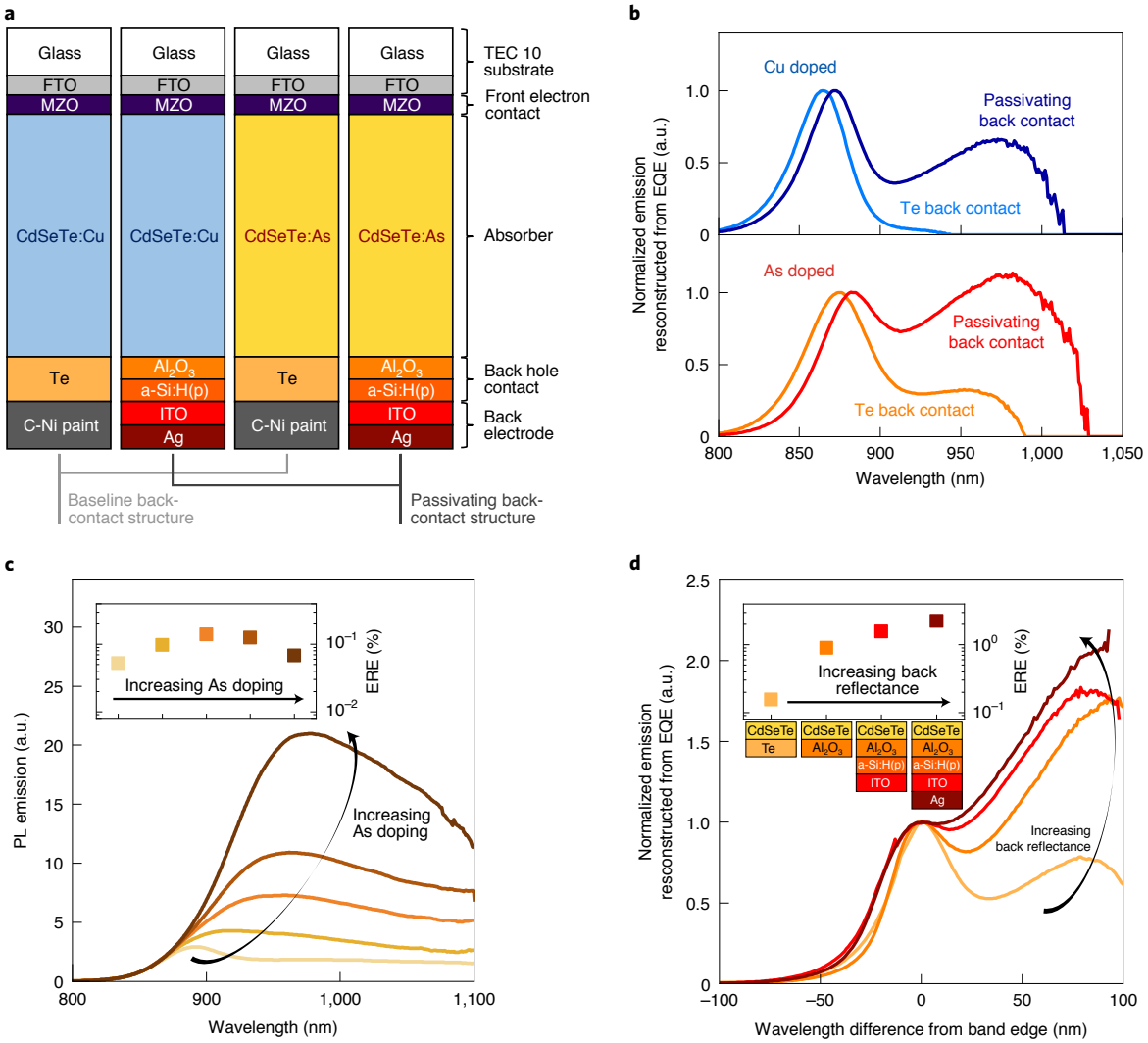

Fig. 1 | Impact of dopant species and back-contact structure on sub-band-gap features. a, General layer structure of the devices reported in this study. **b**, Characteristic sub-band-gap signatures of samples with the combinations of dopant species and back-contact structures used. **c**, Effect of As-doping density on sub-band-gap features in test structures (without back contact) provided by First Solar. The maximum ERE measured for each sample is shown in the inset. **d**, Effect of adding successive layers to form the passivating back-contact stack (the device structure referring to each curve is reported on the *x* axis of the inset) on sub-band-gap features in the case of As-doped devices. For clarity, the reconstructed emission spectra are normalized in amplitude and in wavelength at the lower wavelength band-edge peak. A copy of this figure on a standard 800–1,000 nm wavelength scale is shown in Supplementary Fig. 8. The maximum ERE measured from each sample is, again, shown in the inset. a.u., arbitrary units.

to an improvement of the internal cell optics rather than to a degradation of the cell's material properties. Hence, worse sub-band-gap features do not necessarily mean worse devices: they can just be the consequence of superior cell optics[40].

Impact of doping and back contact on ERE. The ERE values of CdSeTe samples fabricated over two years are presented in Fig. 2. The scale for the corresponding non-radiative recombination loss, $V_{oc,ideal} - iV_{oc}$ is also displayed. As shown in Fig. 2a, the ERE—obtained from calibrated PL measurements (Methods)—correlates with the characteristic decay time $\tau_{TRPL\text{-}tail}$ of the time-resolved photoluminescence (TRPL) tail, which is an excellent estimate of the minority-carrier lifetime τ, provided that the lifetime and the acceptor concentration N_A remain moderate (see Methods and Supplementary Methods 3 for details). The most luminescent samples exhibit remarkably high ERE (>1%), which is on a par with the best crystalline silicon, perovskite and copper indium gallium diselenide solar cells, and long TRPL-tail characteristic decay time ($\tau_{TRPL\text{-}tail} > 1\,\mu s$)[41]. The blue, orange and red regions correspond to the minority-carrier lifetimes τ modelled for given ranges of acceptor concentration N_A, as detailed in the caption to Fig. 2a. The details of our model can be found in Supplementary Methods 2.

Figure 2b compares the iV_{oc} obtained from ERE measurements against the iV_{oc} modelled from experimentally measured $\tau_{TRPL\text{-}tail}$ and N_A, with the former extracted from TRPL measurements and the latter assessed through capacitance–voltage (C–V) measurements, for the devices for which all three measurements (ERE, TRPL, C–V) were performed. Both approaches agree within ±20 mV, with most data points falling within ±10 mV. Thus, improvements in $\tau_{TRPL\text{-}tail}$ and N_A lead to the expected increase in iV_{oc} even though, as discussed in the next section, these do not necessarily translate into an increase in V_{oc}. Higher acceptor concentration devices ($N_A > 3 \times 10^{15}\,cm^{-3}$) are not shown in Fig. 2b, as the TRPL-tail characteristic decay time $\tau_{TRPL\text{-}tail}$ diverges from the actual minority-carrier

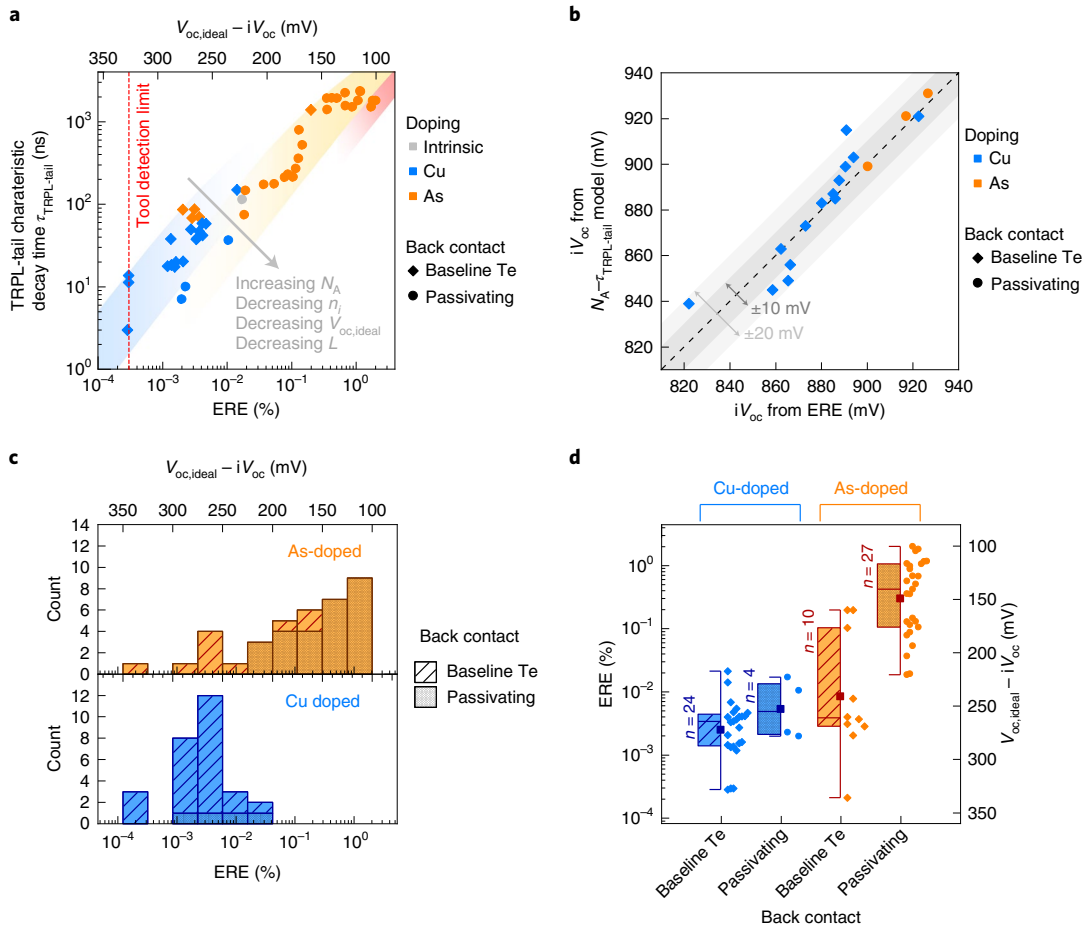

Fig. 2 | ERE of CdSeTe devices fabricated with varying dopant species and back contacts. a, Correlation between ERE and the TRPL-tail characteristic decay time $\tau_{TRPL-tail}$. The highlighted regions correspond to the modelled relationship between ERE and lifetime for $N_A = 2\times10^{14}$ to 2×10^{15} cm^{-3} (blue region), $N_A = 8\times10^{14}$ to 8×10^{15} cm^{-3} (orange region) and $N_A = 8\times10^{15}$ to 2×10^{16} cm^{-3} (red region). The grey arrow and text indicate the dependence of the relationship between ERE and lifetime on material and device parameters (see full model parameters in Supplementary Table 2). **b**, iV_{oc} calculated from ERE versus iV_{oc} modelled from the TRPL-tail characteristic decay time $\tau_{TRPL-tail}$ and the acceptor concentrations N_A (from C–V) for the subset of samples for which all three measurements were performed. The dashed line is the $y = x$ equality line and the dark grey and light grey shaded regions correspond to the areas were the results match within ±10 mV and ±20 mV, respectively. **c**, Distribution of ERE values as a function of the dopant species and the back contact used. Each count corresponds to an individual sample, for which we report the mean ERE. **d**, Statistical analysis of the ERE values as a function of the dopant species and the type of back contact. Each data point (round- and diamond-shaped dots) corresponds to an individual sample, for which we report the mean ERE. The box plot represents the second and third quartiles (25–75% of samples), with the median shown as a horizontal line and the mean shown as a square dot. The whiskers represent the minima and maxima. For each condition, the number, n, of samples is indicated to the left of the box plot.

lifetime τ at high N_A (see Methods and Supplementary Methods 3 for details)[42,43]. A version of Fig. 2b including these outliers is shown in Supplementary Fig. 9, with source data in Supplementary Data 2.

One strong advantage of using the ERE technique to determine iV_{oc} is that only one measurement is needed, with minimal post-treatment of data required, minimal underlying assumptions and minimal restrictions for the sample (that is, C–V measurements cannot be performed on 'unfinished devices', such as cell precursors and passivated films). Furthermore, ERE measurements are taken under steady-state 1-sun-equivalent illumination using a wide-area white bias light, thus better simulating the cell operating conditions than TRPL, where advanced modelling is required to access the exact injection at each point of the decay and to deconvolute transient phenomena, such as carrier separation and diffusion.

Distributions of ERE values can be found in Fig. 2c,d, as a function of the dopant species and the type of back contact used. Passivating back contacts lead to a limited increase in ERE in Cu-doped devices: the ERE is 2.1 times higher on average than for baseline Te back contacts, corresponding to a 20 mV reduction in voltage losses due to non-radiative recombination ($V_{oc,ideal} - iV_{oc}$). Similarly, switching from Cu doping to As doping in samples with a baseline Te back contact yields only an average 3.4 times improvement in ERE, corresponding approximately to a 30 mV reduction in $V_{oc,ideal} - iV_{oc}$. On the other hand, combining As doping with a passivating back contact leads to a substantial improvement in ERE: 36 times average increase (>90 mV decrease in $V_{oc,ideal} - iV_{oc}$) compared to As doping alone; 57 times average increase (>100 mV decrease in $V_{oc,ideal} - iV_{oc}$) compared to using a passivating back contact alone; and 121 times average increase (>120 mV decrease in $V_{oc,ideal} - iV_{oc}$) compared to conventional Cu-doped samples with a baseline Te back contact. These trends have been consistently observed within each batch of devices that we have fabricated and measured. This indicates that, in conventional CdSeTe devices, the iV_{oc} is limited by both the material quality of Cu-doped CdSeTe (that is, bulk recombination) and the poor surface passivation of baseline Te back contacts (that is, back interface recombination). Both recombination

pathways must be mitigated in parallel to substantially improve iV_{oc}: As-doped devices with a baseline Te back contact are still limited by recombination at the back interface, and Cu-doped devices with a passivating back contact are still limited by bulk recombination on Cu-induced defects.

Comprehensive voltage loss breakdown. The full voltage loss analysis for six characteristic samples fabricated at Colorado State University—three Cu doped, three As doped—is displayed in Fig. 3a. Each sample comprises 7 to 25 devices, fabricated simultaneously on the same substrate. The leftmost data correspond to a high-voltage (860–875 mV) high-efficiency (>20%) Cu-doped sample with a baseline Te back contact, among the best set of devices made at Colorado State University. Because of the differences in sub-band-gap behaviours previously discussed, As-doped samples exhibit a reduction of $V_{oc,ideal}$ (referred to as 'radiative emission losses'[44]), which is exacerbated in the presence of a reflective passivating back contact, reaching 65–75 mV in the worst case presented here. Nevertheless, the superior luminescence (ERE) achieved when combining As doping with passivating back contacts more than offsets these losses. As a result, we demonstrate iV_{oc} values exceeding 970 mV, more than 80 mV higher than the V_{oc} of the record-efficiency CdSeTe solar cell[45]. The devices from the best Cu-doped sample reported here (leftmost data points in Fig. 3a) also exhibit relatively high iV_{oc} (920–950 mV), tens of millivolts above the V_{oc} of record-efficiency devices.

Selectivity losses can be visually quantified by the difference between iV_{oc} (upward-pointing triangle) and V_{oc} (downward-pointing triangle) in Fig. 3a. The associated selectivity metric $S_{oc} = V_{oc}/iV_{oc}$ is reported in Supplementary Fig. 10. Among Cu-doped samples—all three of them fabricated with a baseline Te back contact—the 20%-efficient sample exhibits the highest iV_{oc} but also the highest selectivity loss (approximatively 65 mV, $S_{oc} = 0.93$). Since a poor selectivity stems from either a poor passivation or a poor conductivity, we conclude that one of the two contacts in these samples is resistive to the carriers it should be extracting[31]. The two other Cu-doped samples demonstrate an example where V_{oc} is approximatively the same (averages within 10 mV of each other, with overlap of the distributions) but iV_{oc} differs appreciably (>20 mV difference between the averages, with no overlap of the distributions). Thus, these samples achieve similar V_{oc} for different reasons: the first exhibits lower non-radiative recombination (that is, higher *ERE*), whereas the second achieves higher selectivity.

In comparison, the As-doped sample with a baseline Te back contact presents a substantially lower selectivity ($iV_{oc} - V_{oc} > 120$ mV, $S_{oc} = 0.86$). This is again surprising, as the higher N_A obtained with As doping should increase both the hole conductivity and the electron resistivity in the vicinity of the back interface, which should lead to an increase in selectivity[30,31]. Extraction barriers within the absorber (for example, along grain boundaries) could potentially explain this poor selectivity. As shown in Supplementary Fig. 11 and Supplementary Data 3, the wider band gap of CdTe and the graded Cu profile—due to the post-deposition Cu diffusion process—at the back of the device appear to play a key role in the superior selectivity of Cu-doped samples; all else being identical, CdSeTe:As/CdTe/Te devices on which a light Cu-doping treatment is performed achieve a substantially higher selectivity (without iV_{oc} loss) than CdSeTe:As/CdTe/CdSeTe:As/Te devices. Hence, the absorber also plays a role in the selectivity of the device, and it must be optimized to ensure unimpeded carrier extraction.

Finally, the selectivity of As-doped devices with a passivating back contact is quite poor ($iV_{oc} - V_{oc} > 500$ mV, $S_{oc} < 0.5$), thus severely limiting the performance of these devices. As shown in Fig. 3b,c, the selectivity of Cu-doped devices with a passivating back contact is also poor, with $V_{oc} < 500$ mV. This indicates that these passivating back contacts are highly resistive to electrons (which is desirable), but also to holes (which is detrimental). Hence, these contact structures block the extraction of both types of charge carriers. The associated devices often exhibit poor short-circuit current densities (J_{sc}) and EQE, confirming the presence of a carrier-extraction barrier. Considering that similar a-Si:H-based contact structures have enabled $V_{oc} > 1$ V in monocrystalline n-type CdTe solar cells, this behaviour is not expected nor understood[34]. We suspect that this resistivity to holes originates from Fermi-level pinning at the CdSeTe/Al_2O_3 or the Al_2O_3/a-Si:H interface, or from a chemical alteration of the contact during $CdCl_2$ treatment. Given that, when compared with monocrystalline CdSeTe, a stronger space-charge field is observed in Al_2O_3-passivated polycrystalline CdSeTe, the hypothesis of Fermi-level pinning at the interface between polycrystalline CdSeTe and Al_2O_3 is favoured[5].

Notably, all the devices reported in Fig. 3a exhibit non-negligible selectivity losses, ranging from 30–65 mV for conventional Cu-doped devices with a baseline Te back contact, to several hundreds of millivolts for As-doped devices with a passivating back contact. Beyond these six samples, we have not encountered any sample fabricated at Colorado State University for which V_{oc} matched iV_{oc}. This is striking, as V_{oc} closely matches iV_{oc} (within 5 mV or below) under 1-sun illumination for mature crystalline silicon solar cell technologies[46,47], and similar V_{oc}–iV_{oc} matching has recently been demonstrated with perovskite solar cells[11]. Thus, the assumption that $V_{oc} = iV_{oc}$ in CdSeTe solar cells cannot be taken for granted and probably depends on the entire cell fabrication process.

Devices fabricated at First Solar with variable levels of As doping and a ZnTe back contact, reported in Fig. 4, offer a point of comparison where the process-dependent nature of the $V_{oc} = iV_{oc}$ assertion is clearly evident. First Solar has reported similar As-doped solar cells with V_{oc} exceeding 850 mV, acceptor concentrations in the range of 10^{16} cm^{-3} and long-term stability[8,9]. As discussed above, increasing As doping leads to a reduction in $V_{oc,ideal}$ due to increased sub-band-gap features. This, combined with the decrease in ERE at higher As-doping levels—a phenomenon that is probably due to increased dopant compensation—leads to a reduction in iV_{oc} with increasing As doping. The selectivity, conversely, improves steadily with As incorporation, with S_{oc} reaching unity ($V_{oc} = iV_{oc}$) when the As doping is high enough (Supplementary Fig. 12). This result is expected; the higher hole concentration and lower electron concentration at the back of the absorber leads to a high ratio of conductivities between holes and electrons and, thus, to a high selectivity. This demonstrates that proper absorber engineering can drive carrier selectivity.

Nevertheless, these high-selectivity devices have iV_{oc} values below 855 mV, tens of millivolts lower than the devices fabricated at Colorado State University. Comparison between films with a free back surface (no back contact) and finished devices fabricated simultaneously at First Solar, shown in Supplementary Figs. 13–16 and Supplementary Data 1, reveals that deposition of the back contact is responsible for a drop in iV_{oc}. In the absence of the back contact, the ERE is higher by up to an order of magnitude (Supplementary Fig. 14 and Supplementary Data 1) and the iV_{oc} is consequently higher by approximately 60 mV (Supplementary Figs. 15 and 16 and Supplementary Data 1). All else being kept identical until deposition of the back contact, either (1) poor back-contact passivation, or (2) a modification of the absorber or the front interface during its deposition, leads to internal voltage losses of at least 60 mV. Thus, in the short term, improving the back contact—by enhancing the back interface passivation or by mitigating the potential detrimental effect of the contact deposition process—is key to achieving voltages around 900 mV with First Solar's As-doped solar cells. However, in samples with a free back surface, addition of an Al_2O_3 passivation layer leads to a limited increase in photoluminescence: 1.25–2 times improvement, translating into an iV_{oc} increase of 20 mV at best (Supplementary Fig. 17)[48]. This suggests

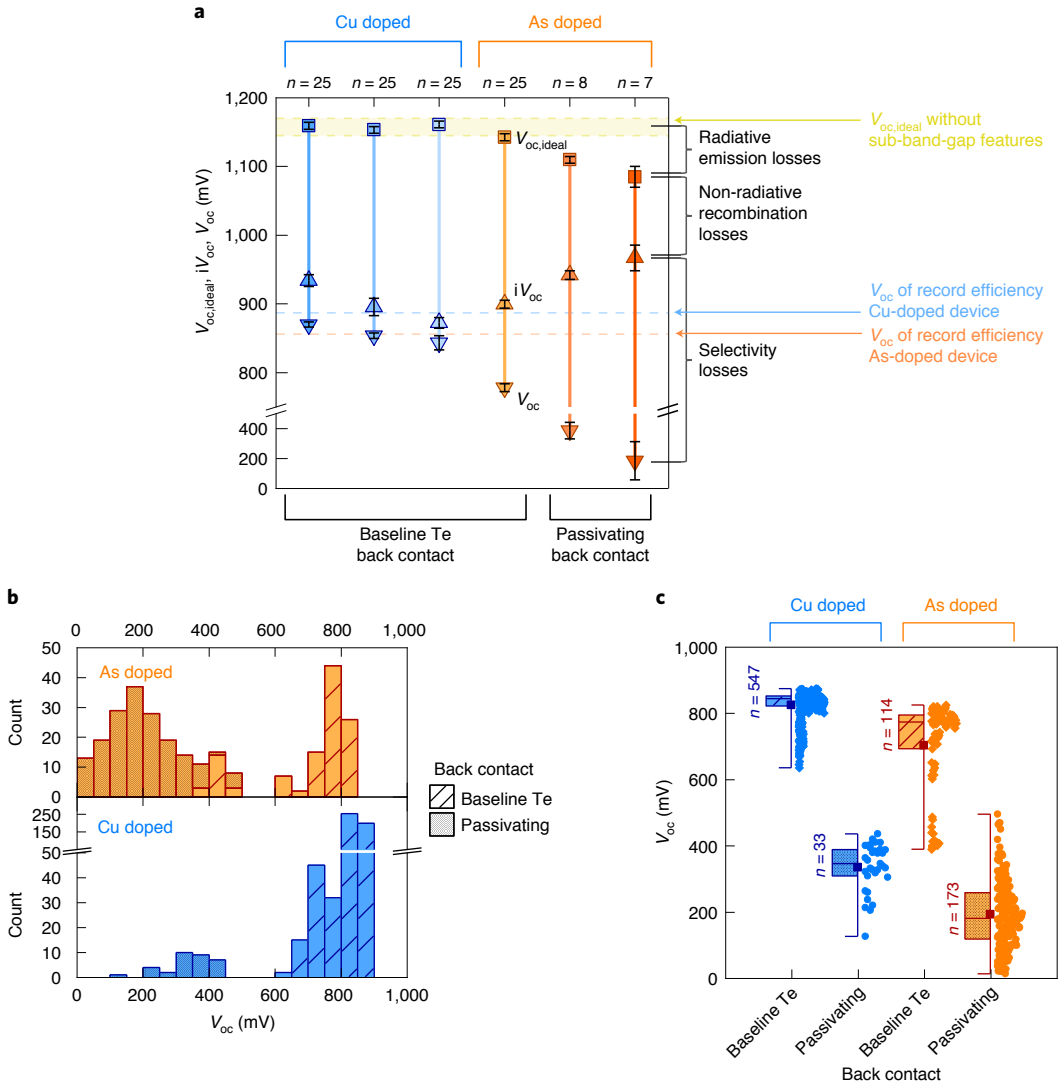

Fig. 3 | Voltage loss analysis of As-doped and Cu-doped CdSeTe samples using baseline Te and passivating back contacts fabricated at Colorado State University. a, Detailed voltage loss analysis for six characteristic samples. The colour shade qualitatively indicates the sample selectivity ($S_{oc} = V_{oc}/iV_{oc}$), from lower selectivity samples (darker shade) to higher selectivity samples (lighter shade). Each sample comprises $n = 7$–25 devices, the exact number of which is indicated at the top of the graph. V_{oc} was measured on each device individually, and the error bars represent the standard deviation of the mean. For each sample, $V_{oc,ideal}$ was determined from the EQE of a representative device, and the error bars represent the uncertainty associated with the measurement. ERE was measured on a representative portion of the devices (3–22, depending on the sample) to calculate iV_{oc} from $V_{oc,ideal}$, and the error bars on iV_{oc} represent the combined uncertainty from the calculation of $V_{oc,ideal}$ and from the standard deviation in the ERE measurement. The range of $V_{oc,ideal}$ obtained in the absence of sub-band-gap features for 1.41–1.44 eV CdSeTe absorbers is indicated, as well as the V_{oc} of record-efficiency As-doped and Cu-doped CdSeTe solar cells. The leftmost data points correspond to a high-voltage (860–875 mV), 20%-efficient sample, among the best set of devices made at Colorado State University. **b**, Distribution of V_{oc} values measured on 869 devices as a function of the dopant species and the back contact used. Each count corresponds to an individual solar cell, with 8 to 25 devices fabricated on each sample plate. **c**, Statistical analysis of the V_{oc} values as a function of the dopant species and the type of back contact. Each data point (round- and diamond-shaped dots) corresponds to an individual solar cell. The box plot represents the second and third quartiles (25–75% of samples), with the median shown as a horizontal line and the mean shown as a square dot. The whiskers represent the minima and maxima. For each condition, the number, *n*, of devices measured is indicated to the left of the box plot.

that, even with a good back-interface passivation, First Solar's current As-doped films are limited to an iV_{oc} around 920–930 mV. To achieve an iV_{oc} (and, subsequently, a V_{oc}) approaching 1 V, sources of recombination other than the absorber/back-contact interface must be tackled. Improvements of the front interface passivation and the bulk absorber material quality are, thus, still needed.

Finally, it is important to note that the iV_{oc}–V_{oc} comparison informs on the combined selectivity of both the electron and hole contacts and does not enable accounting of the selectivity losses due to each contact individually. Further insight into which contact is limiting can be gained only from comparison between devices where one contact is kept identical and the other contact is altered. For example, for samples fabricated at Colorado State University, the MZO front electron contact was kept unchanged across all fabrication runs. As some devices exhibit a reasonably high combined selectivity ($iV_{oc} - V_{oc} < 30$ mV, $S_{oc} = 0.97$), the individual selectivity of MZO is necessarily at least that high. But, for these higher-selectivity devices, we do not have enough information to assign the remaining 30 mV of selectivity losses to one contact or the other. Conversely, for the samples fabricated by First Solar, as a

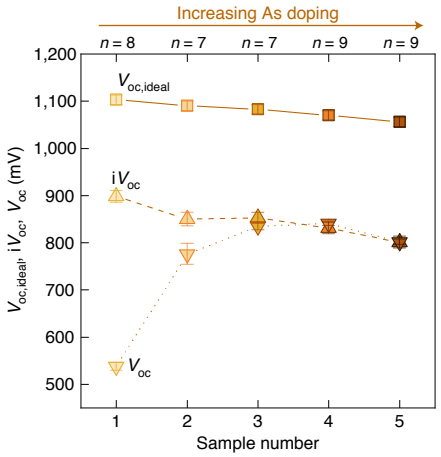

Fig. 4 | Voltage loss analysis of As-doped CdSeTe devices fabricated by First Solar with increasing As incorporation. V_{oc} was measured on $n = 7$–9 devices per sample, as indicated at the top of the graph, and the error bars represent the standard deviation of the mean. For each sample, $V_{oc,ideal}$ was calculated from the absorptance determined from the photoluminescence spectrum of a representative device, as detailed in Supplementary Methods 1, and the error bars represent the uncertainty associated with the measurement. ERE was measured on multiple devices across the samples (17 measurements per sample) to calculate iV_{oc} from $V_{oc,ideal}$, and the error bars on iV_{oc} represent the combined uncertainty from the calculation of $V_{oc,ideal}$ and from the standard deviation in the ERE measurement. For each metric, the line is a guide to the eye.

selectivity equal to unity is achieved at high N_A, we can tentatively assign the entire $iV_{oc} - V_{oc}$ difference at lower As doping to the hole extraction process, with no voltage losses associated with the electron contact (assuming that the change in N_A did not affect the interaction between the front electron contact and the absorber).

Conclusion

The understanding and the improvement of solar cells can be greatly accelerated by performing systematic voltage loss analyses, such as those presented here. By dissecting the origins of voltage losses, one can assess the most effective pathways to improve the performance of photovoltaic devices. Here, we showed that, in the case of CdSeTe devices, the assumption that internal and external voltages match (that is, $V_{oc} = iV_{oc}$) cannot be taken for granted, and the extent of the resulting $iV_{oc} - V_{oc}$ selectivity loss is highly process dependent.

This presents an opportunity and a challenge for Colorado State University's As-doped CdSeTe absorbers with well-passivated interfaces; these samples can achieve ERE values above 1% but, unlike silicon or perovskite solar cells, lack a correspondingly high V_{oc}. Achieving high selectivity ($V_{oc} = iV_{oc}$) with such passivated absorbers—through engineering of the back contact and of its interaction with the absorber—would lead to an increase in V_{oc} of 80 mV over present record-efficiency devices, with the potential of improving the efficiency of CdSeTe solar cells by approximately 2% (absolute) on the basis of voltage gains alone. Similarly, the voltage of First Solar's As-doped devices could be increased by at least 60 mV by improving the back-interface passivation or by reducing the negative impact from the back-contact fabrication process while conserving its excellent selectivity.

Unlocking these potential voltage gains requires engineering contacts that are concurrently passivating and selective, along with ensuring the absence of carrier-extraction barriers within the absorber itself. Among the back-contact candidates investigated here, Te and ZnTe contacts are not passivating enough, whereas Al_2O_3/a-Si:H(p)-based contacts are not selective enough. Research on a passivating carrier-selective back contact is, thus, critical to advance the performance of CdSeTe cells. However, as shown through our voltage loss analysis and suggested by the contrast between a high selectivity and a poor selectivity cell architecture, achieving a V_{oc} exceeding 1 V with CdSeTe solar cells will require research on all the aspects of the device.

Finally, there is room to improve $V_{oc,ideal}$ (and thus iV_{oc} and V_{oc}) by reducing sub-band-gap features. As we have demonstrated, As doping and Se alloying both contribute to these detrimental features, which reduce the thermodynamic voltage limit of the absorber. Engineering the absorber to reduce the concentration of sub-band-gap states without sacrificing the benefits provided by As doping and Se alloying has the potential to substantially improve CdSeTe solar cells and should be an important focus area for future research.

Methods

Sample fabrication. *Substrate preparation and front contact deposition.* Samples fabricated at Colorado State University were deposited on commercially available Pilkington TEC10 substrates, consisting of a 3.2 mm thick soda-lime glass slab, a sodium diffusion barrier and a fluoride-doped tin oxide (FTO) transparent conductive layer. As previously described in the literature[49], before deposition of the absorber, we sputtered a 100 nm thick $Zn_{0.77}Mg_{0.23}O$ electron-contact layer on top of the FTO by planar magnetron sputtering under 5 mTorr pressure in 3%/97% O_2/Ar process gas.

Absorber deposition. The absorbers were deposited by close-space sublimation in the Advanced Research Deposition System (ARDS) at Colorado State University[50]. Unless specified otherwise, the absorbers were deposited as CdSeTe/CdTe bilayers, using either $CdSe_{0.2}Te_{0.8}$ or $CdSe_{0.4}Te_{0.6}$ as the front source material and unalloyed CdTe as the back source material. Se diffusion during the post-deposition $CdCl_2$ activation treatment—also performed in the ARDS tool—leads to the formation of a graded band gap absorber[32]. For select sets of samples, a high-temperature annealing step was performed after the chlorination step.

Absorber doping. Arsenic doping was performed in situ, under Cd overpressure from a stacked secondary sublimation source containing elemental Cd metal, using predoped CdTe, $CdSe_{0.2}Te_{0.8}$ and $CdSe_{0.4}Te_{0.6}$ source materials with As concentrations of 5×10^{17} or 1×10^{20} cm^{-3}. From secondary ion mass spectrometry (SIMS), As concentration in the deposited film reaches 1–10% of the concentration in the source material. As previously described in the literature[50], Cu doping was carried out post-deposition and post-$CdCl_2$ treatment by exposing the grown films to a CuCl vapour source before annealing them, leading to a Cu concentration of 5×10^{17}–2×10^{18} cm^{-3} in the deposited film (again, from SIMS measurements).

Baseline back contact deposition. The baseline Te back contact—consisting of 30–40 nm of Te—was deposited by evaporation in a separate tool following the $CdCl_2$ activation step and eventual Cu-doping process, with a vacuum break during sample transfer. A carbon–nickel conductive electrode was then painted onto the back of the device. Individual devices (7 to 25 per sample, 0.64–0.67 cm^2 in size) were then blast-delineated.

Passivating back contact deposition. Fabrication of the passivating back contact started with the deposition of 2 nm of Al_2O_3 by planar magnetron sputtering under 5 mTorr pressure with 8%/92% O_2/Ar process gas flow, performed at Colorado State University[3]. The samples were then shipped to Arizona State University for deposition of the subsequent layers. An 8 nm layer of p-type boron-doped hydrogenated amorphous silicon (a-Si:H(p)) was deposited by plasma-enhanced chemical vapour deposition in an Applied Material P5000 system. An ITO/Ag (70 nm/200 nm) electrode was then deposited by reactive sputtering in an MRC 944 tool. The samples were then shipped back to Colorado State University where they were blast-delineated into individual devices (7 to 25 per sample, 0.64–0.67 cm^2 in size).

First Solar samples. First Solar's samples are deposited using vapour transport deposition, treated with a $CdCl_2$-based anneal and finished with a ZnTe back contact, as detailed by Metzger et al.[8]. Samples with Al_2O_3 passivation were prepared using atomic layer deposition followed by annealing.

Characterization. *ERE measurement.* ERE measurements were performed at Arizona State University using a modified version of the tool and technique described by Zhao et al. (a schematic of the tool can be found in Supplementary Fig. 18)[51]. The samples were excited with a low-power (<0.05 Sun equivalent) 532 nm diode-pumped solid-state laser, chopped at a frequency of 105–110 Hz, in parallel with a 1-sun-equivalent white light-emitting-diode bias light (not chopped). Emission was detected with a Thorlabs DET10N2 InGaAs photodetector

mounted with a 715 nm absorptive long-pass filter, thus ensuring that no 532 nm excitation photons reflected off the sample could reach the photodetector. Calibration of the excitation photon current was performed with a Spectralon 2% diffuse reflectance standard in the absence of the excitation-blocking long-pass filter. A Stanford Research System SR830 lock-in amplifier was used to extract the chopped PL signal from the background noise.

Spectral photoluminescence. Photoluminescence emission spectra were measured at NREL with a Princeton Instruments HR300 spectrograph and a Pixis400 Si CCD camera, calibrated for spectral sensitivity using calibration lamps provided by the manufacturer. Samples were excited at a wavelength of 632.8 nm using a HeNe continuous-wave laser.

Time-resolved photoluminescence. TRPL measurements were performed at NREL using the time-correlated single-photon counting technique. Samples were excited with 300 fs laser pulses at a wavelength of 640 nm with a 1.1 MHz repetition rate. A low photon fluence per pulse (approximately 10^{12} cm^{-2}) was used to minimize the systematic error due to charging and discharging of the front electron-contact layer, as discussed in Supplementary Methods 3. A Si avalanche photodiode in combination with an interference bandpass filter was used for single-photon detection. For each sample, the TRPL-tail characteristic decay time, $\tau_{\mathrm{TRPL\text{-}tail}}$—which is an excellent estimation of the actual minority-carrier lifetime τ, provided that the lifetime and the acceptor concentration are not too high—was then extracted by fitting the tail of the decay with a single exponential (Supplementary Methods 3). The raw TRPL data for the samples reported in Fig. 2a,b can be found in Supplementary Data 4.

Current density–voltage (J–V) measurements. J–V measurements were performed at room temperature in ambient atmosphere under 1-sun illumination from an ABET Technologies 10600 Xenon arc lamp equipped with an AM1.5G filter, calibrated using a stable CdS/CdTe cell of known J_{sc}. The terminal voltage of the devices was swept from negative (−0.8 V) to positive bias (+1.2 V) in 0.025 V steps with a 4 ms dwell time at each bias while measuring the current through the cells using a Keithley source meter.

EQE measurements. EQE measurements were carried out under illumination from a chopped monochromatic light, selected from a white light source using a monochromator. The solar cell's chopped current response was recorded as a function of wavelength using lock-in amplification. The spectral response of the device was then compared to that of a UV-sensitized crystalline silicon cell of known EQE, measured just before measurement of the devices for calibration purposes.

C–V measurements. C–V measurements were taken at 100 kHz after confirmation that the capacitance was frequency-independent at multiple biases within this frequency range. The amplitude of the voltage oscillation around the measurement voltage was ±10 mV. Capacitance was measured from −1 V to 1 V. Results were analysed using the standard approach from Hegedus and Shafarman, assuming an abrupt junction[52]. Representative carrier concentration versus distance from junction curves for As-doped and Cu-doped samples are displayed in Supplementary Fig. 19. The *C–V* profiles of the samples reported in Fig. 2b can be found in Supplementary Data 5.

Device model. The details and the input parameters of the model used to correlate ERE and τ are presented in Supplementary Methods 2. In Fig. 2a, the shaded regions were calculated from Supplementary equations (17) and (18) using the parameters from Supplementary Table 2. In Fig. 2b, the iV_{oc} was calculated from the TRPL-tail characteristic decay time $\tau_{\mathrm{TRPL\text{-}tail}}$ and the *C–V*-measured acceptor concentration N_A (measured at 0 V bias) using Supplementary equations (14), (15) and (18).

Reporting Summary. Further information on research design is available in the Nature Research Reporting Summary linked to this article.

Data availability

The authors declare that all data supporting the findings of this study are available within the paper and Supplementary Information files. First Solar's data, beyond what is presented in the manuscript and the Supplementary Information, are proprietary and are not publicly available. Source data are provided with this paper.

Received: 15 July 2021; Accepted: 25 January 2022;
Published online: 3 March 2022

References

1. Munshi, A. H. et al. Polycrystalline CdSeTe/CdTe absorber cells with 28 mA/cm^2 short-circuit current. *IEEE J. Photovolt.* **8**, 310–314 (2018).
2. Fiducia, T. A. M. et al. Understanding the role of selenium in defect passivation for highly efficient selenium-alloyed cadmium telluride solar cells. *Nat. Energy* **4**, 504–511 (2019).
3. Kephart, J. M. et al. Sputter-deposited oxides for interface passivation of CdTe photovoltaics. *IEEE J. Photovolt.* **8**, 587–593 (2018).
4. Amarasinghe, M. et al. Mechanisms for long carrier lifetime in Cd(Se)Te double heterostructures. *Appl. Phys. Lett.* https://doi.org/10.1063/5.0047976 (2021).
5. Kuciauskas, D. et al. Recombination velocity less than 100 cm/s at polycrystalline Al_2O_3/CdSeTe interfaces. *Appl. Phys. Lett.* https://doi.org/10.1063/1.5030870 (2018).
6. Kuciauskas, D. et al. in *47th IEEE Photovoltaic Specialists Conference* 82–84 https://doi.org/10.1109/PVSC45281.2020.9300915 (IEEE, 2020).
7. McCandless, B. E. et al. Overcoming carrier concentration limits in polycrystalline CdTe thin films with in situ doping. *Sci. Rep.* **8**, 14519 (2018).
8. Metzger, W. K. et al. Exceeding 20% efficiency with in situ group V doping in polycrystalline CdTe solar cells. *Nat. Energy* **4**, 837–845 (2019).
9. Krasikov, D., Guo, D., Demtsu, S. and Sankin, I. Comparative study of As and Cu doping stability in CdSeTe absorbers. *Sol. Energy Mater. Sol. Cells* https://doi.org/10.1016/j.solmat.2021.111012 (2021).
10. Li, D.-B. et al. Low-temperature and effective ex situ group V doping for efficient polycrystalline CdSeTe solar cells. *Nat. Energy* **6**, 715–722 (2021).
11. Liu, Z. et al. Open-circuit voltages exceeding 1.26 V in planar methylammonium lead iodide perovskite solar cells. *ACS Energy Lett.* **4**, 110–117 (2018).
12. Kayes, B. M. et al. in *37th IEEE Photovoltaic Specialists Conference* 4–8 https://doi.org/10.1109/PVSC.2011.6185831 (IEEE, 2011).
13. Smith, D. D. et al. Toward the practical limits of silicon solar cells. *IEEE J. Photovolt.* **4**, 1465–1469 (2014).
14. Kanevce, A., Reese, M. O., Barnes, T. M., Jensen, S. A. and Metzger, W. K. The roles of carrier concentration and interface, bulk, and grain-boundary recombination for 25% efficient CdTe solar cells. *J. Appl. Phys.* https://doi.org/10.1063/1.4984320 (2017).
15. Duenow, J. N. et al. Relationship of open-circuit voltage to CdTe hole concentration and lifetime. *IEEE J. Photovolt.* **6**, 1641–1644 (2016).
16. Munshi, A. H. et al. in *47th IEEE Photovoltaic Specialists Conference* 1824–1828 https://doi.org/10.1109/PVSC45281.2020.9301003 (2020).
17. Sinton, R. A. & Cuevas, A. Contactless determination of current–voltage characteristics and minority-carrier lifetimes in semiconductors from quasi-steady-state photoconductance data. *Appl. Phys. Lett.* **69**, 2510–2512 (1996).
18. Cuevas, A. & Sinton, R. A. Prediction of the open-circuit voltage of solar cells from the steady-state photoconductance. *Prog. Photovolt. Res. Appl.* **5**, 79–90 (1997).
19. Delamarre, A., Lombez, L. and Guillemoles, J.-F. Contactless mapping of saturation currents of solar cells by photoluminescence. *Appl. Phys. Lett.* https://doi.org/10.1063/1.3697704 (2012).
20. Katahara, J. K. & Hillhouse, H. W. Quasi-Fermi level splitting and sub-bandgap absorptivity from semiconductor photoluminescence. *J. Appl. Phys.* https://doi.org/10.1063/1.4898346 (2014).
21. Sarritzu, V. et al. Optical determination of Shockley-Read-Hall and interface recombination currents in hybrid perovskites. *Sci. Rep.* **7**, 44629 (2017).
22. Stolterfoht, M. et al. The impact of energy alignment and interfacial recombination on the internal and external open-circuit voltage of perovskite solar cells. *Energ. Environ. Sci.* **12**, 2778–2788 (2019).
23. Ruppel, W. & Würfel, P. Upper limit for the conversion of solar energy. *IEEE Trans. Electron Devices* **27**, 877–882 (1980).
24. Shockley, W. & Queisser, H. J. Detailed balance limit of efficiency of p-n junction solar cells. *J. Appl. Phys.* **32**, 510–519 (1961).
25. Jean, J. et al. Radiative efficiency limit with band tailing exceeds 30% for quantum dot solar cells. *ACS Energy Lett.* **2**, 2616–2624 (2017).
26. Vandewal, K., Tvingstedt, K., Gadisa, A., Inganas, O. & Manca, J. V. On the origin of the open-circuit voltage of polymer–fullerene solar cells. *Nat. Mater.* **8**, 904–909 (2009).
27. Miller, O. D., Yablonovitch, E. & Kurtz, S. R. Strong internal and external luminescence as solar cells approach the Shockley–Queisser limit. *IEEE J. Photovolt.* **2**, 303–311 (2012).
28. Würfel, P. and Würfel, U. *Physics of Solar Cells: From Basic Principles to Advanced Concepts* 3rd edn (Wiley-VCH, 2016).
29. Würfel, P. The chemical potential of radiation. *J. Phys. C* **15**, 3967–3985 (1982).
30. Würfel, U., Cuevas, A. & Würfel, P. Charge carrier separation in solar cells. *IEEE J. Photovolt.* **5**, 461–469 (2015).
31. Onno, A., Chen, C., Koswatta, P., Boccard, M. & Holman, Z. C. Passivation, conductivity, and selectivity in solar cell contacts: concepts and simulations based on a unified partial-resistances framework. *J. Appl. Phys.* **126**, 183103 (2019).
32. Munshi, A. H. et al. Effect of $CdCl_2$ passivation treatment on microstructure and performance of CdSeTe/CdTe thin-film photovoltaic devices. *Sol. Energy Mater. Sol. Cells* **186**, 259–265 (2018).
33. Danielson, A. et al. in *46th IEEE Photovoltaic Specialists Conference* 3018–3023 https://doi.org/10.1109/PVSC40753.2019.8980466 (IEEE, 2019).

34. Zhao, Y. et al. Monocrystalline CdTe solar cells with open-circuit voltage over 1 V and efficiency of 17%. *Nat. Energy* **1**, 16067 (2016).
35. De Wolf, S., Descoeudres, A., Holman, Z. C. & Ballif, C. High-efficiency silicon heterojunction solar cells: a review. *Green* **2**, 7–24 (2012).
36. Zhao, X.-H. et al. Determination of CdTe bulk carrier lifetime and interface recombination velocity of CdTe/MgCdTe double heterostructures grown by molecular beam epitaxy. *Appl. Phys. Lett.* https://doi.org/10.1063/1.4904993 (2014).
37. Zhao, X.-H. et al. Time-resolved and excitation-dependent photoluminescence study of CdTe/MgCdTe double heterostructures grown by molecular beam epitaxy. *J. Vac. Sci. Technol. B* https://doi.org/10.1116/1.4878317 (2014).
38. Moseley, J. et al. Impact of dopant-induced optoelectronic tails on open-circuit voltage in arsenic-doped Cd(Se)Te solar cells. *J. Appl. Phys.* https://doi.org/10.1063/5.0018955 (2020).
39. Grover, S. et al. in *44th IEEE Photovoltaic Specialists Conference* 1193–1195 https://doi.org/10.1109/PVSC.2017.8366147 (IEEE, 2017).
40. Onno, A. et al. in *48th IEEE Photovoltaic Specialists Conference* 1754–1757 https://doi.org/10.1109/PVSC43889.2021.9518829 (IEEE, 2021).
41. Green, M. A. & Ho-Baillie, A. W. Y. Pushing to the limit: radiative efficiencies of recent mainstream and emerging solar cells. *ACS Energy Lett.* **4**, 1639–1644 (2019).
42. Moseley, J., Krasikov, D., Lee, C. and Kuciauskas, D. Diverse simulations of time-resolved photoluminescence in thin-film solar cells: A SnO2/CdSeyTe1−y case study. *J. Appl. Phys.* https://doi.org/10.1063/5.0063028 (2021).
43. Jundt, P., Kuciauskas, D. and Sites, J. in *47th IEEE Photovoltaic Specialists Conference* 1408–1412 https://doi.org/10.1109/PVSC45281.2020.9300522 (IEEE, 2020).
44. Guillemoles, J.-F., Kirchartz, T., Cahen, D. & Rau, U. Guide for the perplexed to the Shockley–Queisser model for solar cells. *Nat. Photonics* **13**, 501–505 (2019).
45. Green, M. et al. Solar cell efficiency tables (version 57). *Prog. Photovolt. Res. Appl.* **29**, 3–15 (2020).
46. Dumbrell, R., Juhl, M. K., Trupke, T. & Hameiri, Z. Comparison of terminal and implied open-circuit voltage measurements. *IEEE J. Photovolt.* **7**, 1376–1383 (2017).
47. Bivour, M. et al. in *33rd European PV Solar Energy Conference* (eds Smets, A. et al.) (Curran Associates, 2018).
48. Grover, S. in *4th CdTe workshop* (2020).
49. Kephart, J. M. et al. Band alignment of front contact layers for high-efficiency CdTe solar cells. *Sol. Energy Mater. Sol. Cells* **157**, 266–275 (2016).
50. Swanson, D. E. et al. Single vacuum chamber with multiple close space sublimation sources to fabricate CdTe solar cells. *J. Vac. Sci. Technol. A* **34**, 021202 (2016).
51. Zhao, Y., Zhao, X.-H. and Zhang, Y.-H. in *43rd IEEE Photovoltaic Specialists Conference* 545–548 https://doi.org/10.1109/PVSC.2016.7749654 (IEEE, 2016)
52. Hegedus, S. S. & Shafarman, W. N. Thin-film solar cells: device measurements and analysis. *Prog. Photovolt. Res. Appl.* **12**, 155–176 (2004).

Acknowledgements

The information, data or work presented herein was funded in part by the US Department of Energy, Office of Energy Efficiency and Renewable Energy, under award numbers DE-EE0008552 (A.O., C.L., S.L., A.D., W.W., A.B., D.K., W.S. and Z.C.H.) and DE-EE0008557 (C.L. and W.S.). Funding was provided in part by the National Science Foundation under award no. 1846685 (Z.C.H.). This work was authored in part by the National Renewable Energy Laboratory, operated by Alliance for Sustainable Energy, LLC, for the US Department of Energy (DOE) under contract no. DE-AC36-08GO28308 (D.K.). The views expressed herein do not necessarily represent the views of the DOE or the US Government. The US Government retains and the publisher, by accepting the article for publication, acknowledges that the US Government retains a nonexclusive, paid-up, irrevocable, worldwide license to publish or reproduce the published form of this work, or allow others to do so, for US Government purposes. We thank Y.-H. Zhang and his team at Arizona State University for building and providing access to the ERE measurement tool and J. Sites and his team at Colorado State University for building and providing access to the EQE and C–V measurement tools. We thank R. Pandey, T. Shimpi and J. Sites at Colorado State University, along with G. Yeung and C. Wolden at Colorado School of Mines, for providing some of the samples reported in this study. We thank 5N Plus for providing the CdTe, CdSeTe and $CdCl_2$ source materials. First Solar authors acknowledge support from numerous colleagues and thank D. Martinez and K. Theis for sample preparation and analysis.

Author contributions

A.O. and Z.C.H. conceived the project. A.O., C.R., A.D., S.G. and D.K. designed the methodology. A.O., C.R., S.L. and D.K. performed the formal analysis. A.O., C.R., S.L., A.D., W.W., A.B., S.G., J.B. and D.K. carried out the investigations. S.G., D.K., W.S. and Z.C.H. provided resources. A.O. wrote the original draft and A.O., C.R., A.D., A.B., S.G., D.K., W.S. and Z.C.H. reviewed and edited the manuscript. A.O. performed the visualization. D.K., W.S., G.X. and Z.C.H. supervised the project. A.O., D.K., W.S. and Z.C.H. acquired funding.

Competing interests

S.G., J.B. and G.X. work at First Solar, which is a publicly traded company that manufactures CdTe solar modules. Outside of this, the authors declare no competing interests.

Additional information

Supplementary information The online version contains supplementary material available at https://doi.org/10.1038/s41560-022-00985-z.

Correspondence and requests for materials should be addressed to Arthur Onno or Zachary C. Holman.

Peer review information *Nature Energy* thanks the anonymous reviewers for their contribution to the peer review of this work.

Reprints and permissions information is available at www.nature.com/reprints.

Publisher's note Springer Nature remains neutral with regard to jurisdictional claims in published maps and institutional affiliations.

Corresponding author(s): Arthur Onno; arthur.onno@asu.edu

Solar Cells Reporting Summary

Nature Research wishes to improve the reproducibility of the work that we publish. This form is intended for publication with all accepted papers reporting the characterization of photovoltaic devices and provides structure for consistency and transparency in reporting. Some list items might not apply to an individual manuscript, but all fields must be completed for clarity.

For further information on Nature Research policies, including our data availability policy, see Authors & Referees.

Experimental design

Please check: are the following details reported in the manuscript?

1. Dimensions			
Area of the tested solar cells	☒ Yes ☐ No	0.64–0.67 cm², as detailed in the Methods – Sample fabrication section
Method used to determine the device area	☒ Yes ☐ No	Devices blast-delineated through a mask as detailed in the Methods – Sample fabrication section
2. Current-voltage characterization			
Current density-voltage (J-V) plots in both forward and backward direction	☐ Yes ☒ No	Hysteresis not observed
Voltage scan conditions *For instance: scan direction, speed, dwell times*	☒ Yes ☐ No	J–V curve independent of voltage scan conditions. Scan from negative (-0.8V) to positive bias (+1.2 V) in 0.025 V steps with a 4 ms dwell at each bias, as detailed in the Methods – Characterization section
Test environment *For instance: characterization temperature, in air or in glove box*	☒ Yes ☐ No	Cells characterized in ambient atmosphere at room temperature, as detailed in the Methods – Characterization section
Protocol for preconditioning of the device before its characterization	☐ Yes ☒ No	No need to pre-condition devices before measurements.
Stability of the J-V characteristic *Verified with time evolution of the maximum power point or with the photocurrent at maximum power point; see ref. 7 for details.*	☐ Yes ☒ No	No short-term degradation in J–V characteristic observed with CdSeTe solar cells. Long-term degradation not the subject of this study.
3. Hysteresis or any other unusual behaviour			
Description of the unusual behaviour observed during the characterization	☐ Yes ☒ No	Hysteresis not observed
Related experimental data	☐ Yes ☒ No	Hysteresis not observed
4. Efficiency			
External quantum efficiency (EQE) or incident photons to current efficiency (IPCE)	☒ Yes ☐ No	Detailed in the Methods – Characterization section
A comparison between the integrated response under the standard reference spectrum and the response measure under the simulator	☐ Yes ☒ No	Current density losses not the subject of this contribution.
For tandem solar cells, the bias illumination and bias voltage used for each subcell	☐ Yes ☒ No	Not tandem cells.
5. Calibration			
Light source and reference cell or sensor used for the characterization	☒ Yes ☐ No	Detailed in the Methods – Characterization section J–V measurements performed under 1-sun illumination from an ABET Technologies 10600 Xenon Arc lamp equipped with an AM1.5G filter, calibrated using a stable CdS/CdTe cell of known Jsc.

Confirmation that the reference cell was calibrated and certified	☐ Yes ☒ No	Reference cell not certified but current density is not the subject of our manuscript. Jsc of the calibration cell has been measured at NREL periodically to verify stability.
Calculation of spectral mismatch between the reference cell and the devices under test	☐ Yes ☒ No	Spectral mismatch not calculated. Again, current density is not the subject of this contribution.

6. Mask/aperture

Size of the mask/aperture used during testing	☐ Yes ☒ No	No mask used. Current density is not the subject of this contribution.
Variation of the measured short-circuit current density with the mask/aperture area	☐ Yes ☒ No	No mask used. Current density is not the subject of this contribution.

7. Performance certification

Identity of the independent certification laboratory that confirmed the photovoltaic performance	☐ Yes ☒ No	No record efficiency reported here, paper focuses on voltage loss analysis.
A copy of any certificate(s) *Provide in Supplementary Information*	☐ Yes ☒ No	No record efficiency reported here, paper focuses on voltage loss analysis.

8. Statistics

Number of solar cells tested	☒ Yes ☐ No	Caption of Figures 5 and 6. Sample comprises 8 to 25 cells, Voc measured on at least 7 devices, ERE measured on a representative portion of the devices (3 to 22 depending on sample size).
Statistical analysis of the device performance	☒ Yes ☐ No	Figure 4c, 4d, 5, and 6.

9. Long-term stability analysis

Type of analysis, bias conditions and environmental conditions *For instance: illumination type, temperature, atmosphere humidity, encapsulation method, preconditioning temperature*	☐ Yes ☒ No	Long-term degradation not the subject of this study.